Letter

Evidence for reduced periodic lattice distortion within the Sb-terminated surface layer of the kagome metal CsV_3Sb_5

Felix Kurtz,[1,2] Gevin von Witte,[1,3,4] Lukas Jehn,[1,2] Alp Akbiyik,[1,2] Igor Vinograd,[1,2] Matthieu Le Tacon,[5] Amir A. Haghighirad,[5] Dong Chen,[6] Chandra Shekhar,[6] Claudia Felser,[6] and Claus Ropers[1,2,*]

[1]*Max Planck Institute for Multidisciplinary Sciences, 37077 Göttingen, Germany*
[2]*4th Physical Institute – Solids and Nanostructures, University of Göttingen, 37077 Göttingen, Germany*
[3]*Institute for Biomedical Engineering, University and ETH Zurich, 8092 Zurich, Switzerland*
[4]*Institute of Molecular Physical Science, ETH Zurich, 8093 Zurich, Switzerland*
[5]*Institute for Quantum Materials and Technologies, Karlsruhe Institute of Technology, 76021 Karlsruhe, Germany*
[6]*Max Planck Institute for Chemical Physics of Solids, 01187 Dresden, Germany*

(Received 3 December 2024; revised 13 February 2025; accepted 12 March 2025; published 9 April 2025)

The discovery of the kagome metal CsV_3Sb_5 sparked broad interest, due to the coexistence of a charge density wave (CDW) phase and possible unconventional superconductivity in the material. In this Letter, we use low-energy electron diffraction (LEED) with a μm-sized electron beam to explore the periodic lattice distortion at the antimony-terminated surface in the CDW phase. We recorded high-quality backscattering diffraction patterns in ultrahigh vacuum from multiple cleaved samples. Unexpectedly, we did not find superstructure reflexes at intensity levels predicted from dynamical LEED calculations for the reported $2 \times 2 \times 2$ bulk structure. Our results suggest that in CsV_3Sb_5 the periodic lattice distortion accompanying the CDW is less pronounced at Sb-terminated surfaces than in the bulk.

DOI: 10.1103/PhysRevB.111.L140101

A new family of superconducting kagome materials has recently attracted much attention due to the rich phenomenology they offer, including a band structure containing a flat band, a Dirac cone, and multiple van Hove singularities [1,2]. The vanadium-based kagome materials AV_3Sb_5 with $A =$ (Rb, K, Cs) exhibit superconductivity at ambient pressure below temperatures $T_c \approx 0.75$, 0.93, and 2.5 K, respectively [3–5]. Remarkably, the superconducting phase emerges within a charge-ordered state with a 2×2 motif of the charge density wave (CDW). The CDW in the kagome layers onsets at much higher temperatures of $T_{CDW} = 78$–103 K. Significant effort has been devoted to uncovering the mechanism behind CDW formation. Band-structure calculations indicate that strong electron-phonon coupling renders the lattice unstable [6]. However, a phonon softening at the CDW wave vector, as expected for a Peierls-like mechanism, was not observed experimentally [7]. An electron-driven nesting of the high density of states at saddle points located at the M points on the Brillouin zone boundary would lead to the observed 2×2 motif. However, two-dimensional (2D) Fermi-surface nesting as a driving mechanism of the CDW has been questioned [8,9], rather accentuating the interlayer coupling which leads to out-of-plane stacking with $2 \times 2 \times 2$, or $2 \times 2 \times 4$ supercells [10–16].

As with superconductivity [17], there are reports of an unconventional nature of the CDW, suggesting a state with broken time-reversal symmetry (TRS) [17] despite the absence of static magnetism [1]. This may arise from a complex CDW order parameter that induces orbital currents in the kagome layers [18]. Early scanning tunneling microscopy (STM) and resistivity measurements also observed chirality as well as nematicity in the CDW state [19–21]—effects rarely seen in other CDW materials and suggesting an alternative electronic mechanism that is derived from the unusual kagome band structure [22]. However, it remains unresolved whether TRS breaking [23], orbital currents [24], chirality [25,26], or nematicity [27] indeed occur in these kagome materials. Some of the observed discrepancies may result from intrinsic differences in the surface and bulk properties. Whereas optical conductivity and Raman scattering found CDW gap energies between 80 and 100 meV [28–30], gaps derived from STM and angle-resolved photoemission spectroscopy (ARPES) vary from 20 meV [31,32] to 50–70 meV [33]. Important insights on the surface properties were gained by STM studies that concentrated on the Sb-terminated surface due to its robustness, and which uncovered an additional unidirectional 1×4 stripe order [20,34–36]. To date, the associated structural properties are not known, which calls for crystallographic investigations using surface-sensitive techniques.

In this Letter, we use low-energy electron diffraction (LEED) with a μm-sized electron beam on CsV_3Sb_5 in its CDW phase. We find no diffraction signature of a CDW-coupled periodic lattice distortion (PLD) on the Sb-terminated

*Contact author: claus.ropers@mpinat.mpg.de

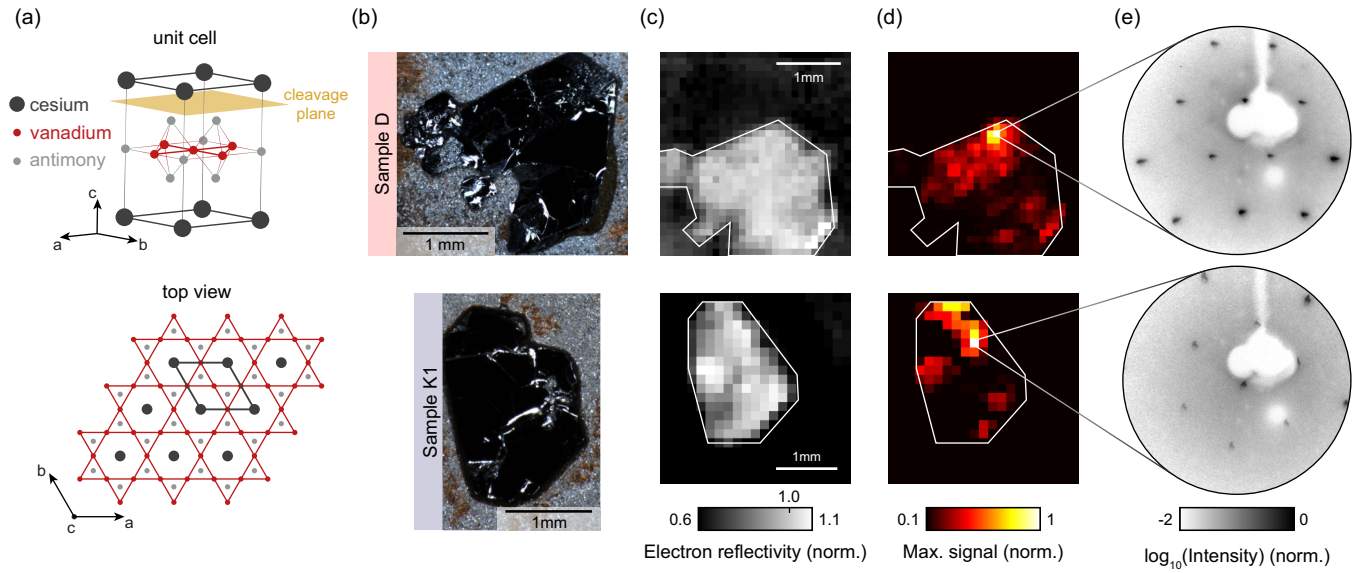

FIG. 1. (a) Crystal structure of CsV_3Sb_5 showcasing a vanadium kagome net. The cleavage plane between cesium and antimony planes is indicated. (b) Optical microscope images of two CsV_3Sb_5 samples. (c) Corresponding spatial scans where each pixel represents the total intensity in the recorded diffraction image (integration time 3 s), resembling the shape of the sample. (d) Same spatial scans where each pixel displays the maximum intensity in the recorded diffraction image, indicating positions of high surface quality and low local curvature resulting in bright and sharp diffraction spots. (e) Diffraction images taken at the areas with high total and maximum intensity (90 eV electron energy, integration times of 20 s in the top image and 30 s in the bottom image, 30 K sample temperature).

surface, while dynamical LEED simulations for the x-ray-determined $2 \times 2 \times 2$ bulk structure predict superstructure peaks well above the noise level in our experiment. The robustness of this observation is tested on several samples from batches of crystals grown at two different institutions. Our observations suggest a reduced lattice distortion at the Sb-terminated surface and highlight the importance of surface-sensitive structural probes to complement the interpretation of electronic properties measured by ARPES or STM.

The material's unit cell consists of four atomic layers, namely a strongly bound V_3Sb_5 stack sandwiched between Cs layers [Fig. 1(a)], with the vanadium atoms arranged in a kagome net. Antimony atoms fill the inner sites of the hexagons and additionally arrange in a honeycomb lattice above and below the kagome layer. As a consequence of the weaker bonding, the cleavage plane is between Cs and Sb planes, creating two possible terminations with either cesium or antimony at the surface.

In the experiments, cleaving multiple samples usually resulted in only small areas of high crystalline quality, and we found it necessary to study the surface with a μm-scale electron beam. In particular, we employed our home-built electron gun with a beam diameter of 80–100 μm [37]. We screened six cleaves of four different crystals for superstructure reflexes. On two cleaved samples, shown in Fig. 1(b), we performed spatial LEED scans. In these measurements, LEED images with an integration time of 3 s were taken across a square grid on the entire sample (pixel spacing 100 and 150 μm, respectively). For every scan position, we display the total reflected electron signal [Fig. 1(c)] and the maximum intensity within the diffraction image [Fig. 1(d)], which indicates the quality and the sharpness of the position-dependent diffraction pattern. Overall, the macroscopic shapes of the crystals are represented by an elevated, comparably homogeneous total electron reflectivity. Yet, only small areas, roughly 200 μm in diameter, yield sharp diffraction images with high peak intensities that imply high surface quality and flatness over the electron beam diameter. Example diffraction images of these high-quality locations are shown in Fig. 1(e) (see also Fig. S1 in the Supplemental Material [38] for LEED images of other locations). Both images are taken with electrons at 90 eV energy, and at a sample temperature of 30 K, significantly below the phase transition temperature, $T_{CDW} = 94$ K. Nonetheless, under these conditions, no evidence for superstructure diffraction peaks is found.

We cleave the crystals at room temperature before cooling, which can lead to two distinct terminations [34], namely a 1×1 antimony termination or a partial $\sqrt{3} \times \sqrt{3}$ cesium termination. Similar observations were made for RbV_3Sb_5 [39]. Some signatures of partial cesium termination are visible by additional spots, faintly seen in the top panel of Fig. 1(e). Yet we note that these $(\sqrt{3} \times \sqrt{3})R30^\circ$ peaks are either very weak or not visible at all, depending on the probed position, suggesting that this termination covers a rather small fraction of the total surface area. Furthermore, these spots disappear when the sample is held at room temperature for several hours, likely due to increased Cs desorption (see Fig. S4 in the Supplemental Material [38]). Overall, these observations indicate that we are dealing primarily with Sb terminations in our measurements. This is further corroborated by electron-energy-dependent measurements in conjecture with dynamical LEED calculations below (Fig. 3).

In order to obtain quantitative predictions of expected superstructure peak intensities associated with the CDW, we perform dynamical LEED calculations in the electron energy

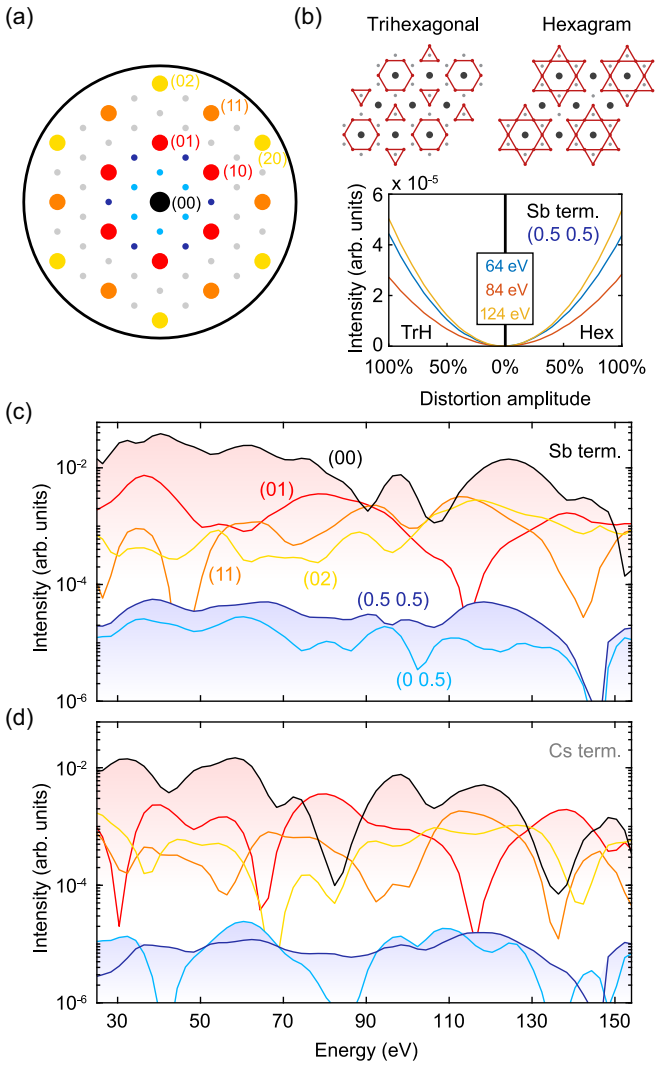

FIG. 2. Dynamical LEED calculations: (a) Schematic LEED pattern with strongest expected superstructure peaks in blue. (b) Quadratic scaling of the diffraction signal with the distortion amplitude, shown here for the Sb termination, the (0.5 0.5) spot, and three different energies. The left side shows the distortion towards the trihexagonal structure, whereas the right side treats the hexagram distortion. (c), (d) Energy-dependent signal strength of the four strongest main-lattice peaks as well as the two strongest CDW peaks for both Cs and Sb terminations, retrieved from dynamical LEED calculations. The distortions are taken from Ref. [11] (trihexagonal).

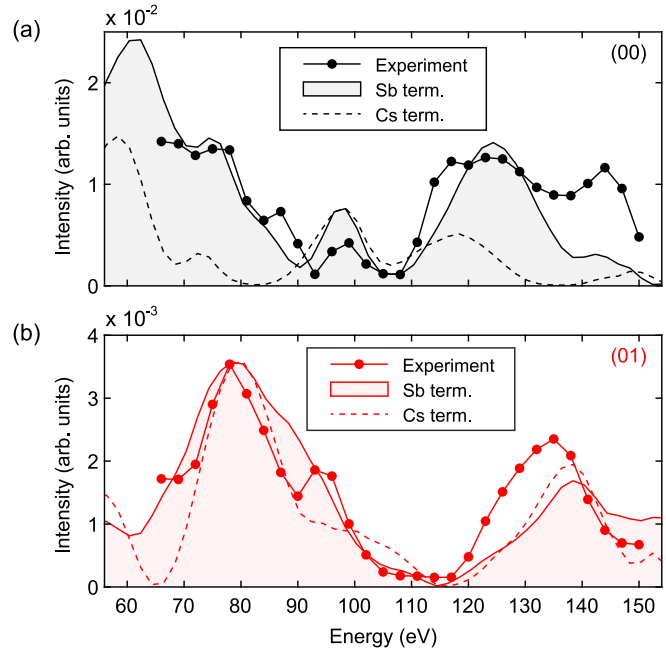

FIG. 3. Experimental spot intensities compared with dynamical LEED calculations, considering the (00) spot in (a) and the (01) spots in (b). The simulations assume either a complete antimony or cesium termination. We find a good agreement with an assumed antimony termination, especially distinguishable from the cesium termination for the (00) spot.

range from 25 to 155 eV (TensErLEED package [40]). In these computations, we assume the $2 \times 2 \times 2$ lattice distortions as obtained from x-ray diffraction in the bulk [11]. Two distinct structural distortions are discussed in the literature: the hexagram distortion (also known as Star-of-David pattern) and its inverse, the trihexagonal distortion [Fig. 2(b), top]. Both distortions produce the 2×2 motif in the kagome plane, while the staggering of either two hexagram or two trihexagonal distortions results in an additional doubling of the unit cell along the vertical direction. The distortion amplitudes for both cases are estimated from the same bulk diffraction data, and thus also show large similarities in our calculations. For simplicity, in the following, we only display the curves for the trihexagonal distortion, which represents the suggested ground state by density functional theory calculations [41,42]. The results for the hexagram distortion are shown in Fig. S2 in the Supplemental Material [38]. In Fig. 2(a), the PLD spots are indicated, and the sixfold symmetry becomes apparent. The energy-dependent spot intensities are displayed in Figs. 2(c) and 2(d) for complete Sb or Cs surface terminations, respectively. We show the specular reflex and the main-lattice peaks of first and second order. Furthermore, the two strongest superstructure spots are shown, which are generally between two and three orders of magnitude less intense than the main spots. In particular, the (0.5 0.5) spot appears nearly energy independent in the range of 40–130 eV, regardless of termination.

Before applying the presented dynamical LEED calculations to the search for superstructure reflexes, we first use them to determine the surface termination in the experiment. Namely, we perform LEED-$I(V)$ measurements, i.e., we record spot intensities as a function of electron energy, on the high-quality surface area of sample D and compare them with the predictions made for either a complete antimony or cesium termination (Fig. 3). Experimentally, we only analyze the spots that are visible throughout the entire energy scan from 66 to 150 eV, namely three (01) spots, over which we average, and the (00) spot. Indeed, we find a fairly good agreement with the Sb-terminated simulation as proposed above, while an assumed Cs termination would lead to a significantly different energy dependence of the (00) spot in particular [the dashed line in Fig. 3(a)]. This can be further illustrated by a logarithmic intensity scale as shown in Fig. S3 in the

Supplemental Material [38], as this termination predicts several electron energies at which the spots should disappear—in stark contrast to the experimental data. Quantitatively, the Pendry R factor indicates a better fit for the (00) spot with antimony termination (0.32) compared to cesium termination (0.75). Both terminations yield an identical R factor of 0.21 for the (01) spot. Combined with the general weakness of the $(\sqrt{3} \times \sqrt{3})R30^\circ$ spots discussed above, we find predominantly antimony-terminated surfaces in our experiments.

After screening several surfaces at various electron energies and finding no indication of superstructure spots, we enhance the signal-to-noise ratio by prolonging the integration time. Based on the predictions of the dynamical LEED calculations, we record diffraction images at a high-quality surface position of sample K2. Using an electron energy of 130 eV, we increase the dynamic range of the measurement by integrating multiple camera frames over an extended duration of 11 min [Fig. 4(a), left]. At this electron energy, first- and second-order main-lattice spots appear at a similar intensity, and multiple locations of potential superstructure peaks are accessible in the diffraction pattern. We now analyze these high-quality backscattering diffraction images, focusing on the search for superstructure peaks. To this end, it is necessary to determine the noise floor. After normalizing with a flat-field image and subtracting a slowly varying background (see Sec. III of the Supplemental Material [38] for further details), we obtain the image shown on the right in Fig. 4(a). To further increase the signal-to-noise ratio, we binned the image considerably such that the observed main-lattice spots cover only a few pixels, as shown in the zoom-in of the (00) spot. Although this substantially increases the sensitivity to faint diffraction features, the measurements do not exhibit signs of a superstructure peak exceeding the remaining noise level. As an example, we depict the region around a (0.5 0.5) location in Fig. 4(b), where a linear intensity gradient within the shown square is subtracted. In order to estimate an upper boundary for the intensity of possibly undetected superstructure peaks, we determine the background noise level. To this end, we create an intensity histogram within a stripe between the main-lattice spots [Fig. 4(c)]. Its standard deviation is $\sigma_{\text{noise}} = 3.3 \times 10^{-4}$ [43]. We define the detection threshold as $3\sigma_{\text{noise}} = 9.9 \times 10^{-4}$, meaning that, under Gaussian noise, only 1.5 out of every 1000 pixels are statistically expected to exceed this threshold. With the spot position known to a precision of up to 5×5 pixels at most, the probability of mistakenly attributing a noise-induced count as a diffraction peak is exceedingly low.

We now compare the obtained detection threshold with the expected superstructure intensities from Fig. 2 by summarizing the different spot intensities in Fig. 4(d). This panel shows the intensities of the (00) and the first- and second-order main-lattice spots, which are determined from the experimental data in the LEED image. Furthermore, the expected (0 0.5) and (0.5 0.5) CDW spot intensities from our dynamical LEED calculations are depicted for an Sb-terminated surface. We hereby consider the sum of all observed main-lattice peaks rather than a single spot as the reference between experiment and simulation. Furthermore, we present the results of the same analysis performed for a diffraction image at 80 eV. As can be seen, all predicted intensities of the displayed CDW

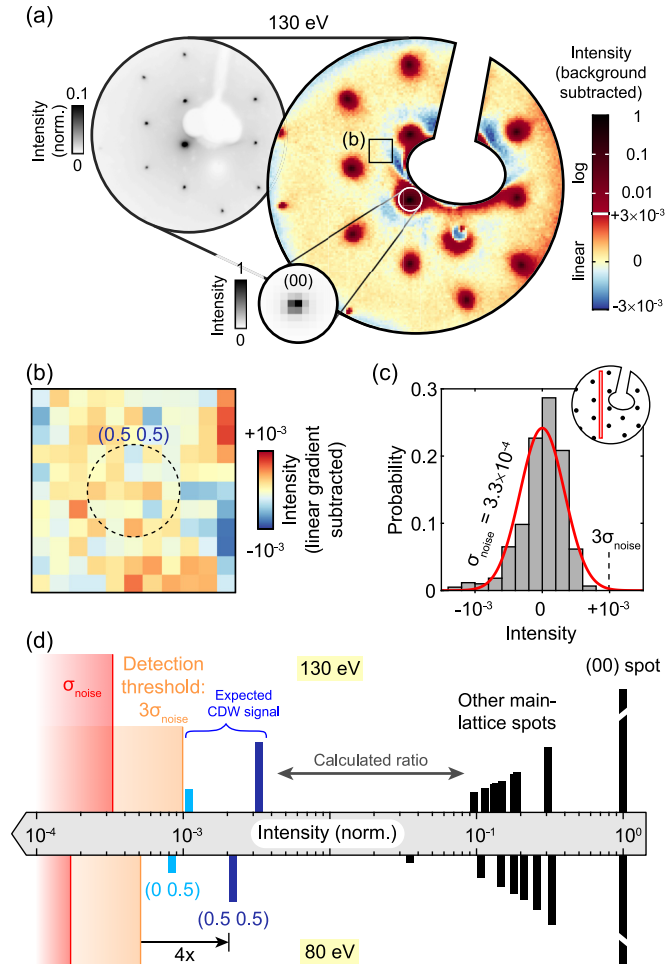

FIG. 4. Search for superstructure peaks and noise analysis: (a) LEED image at 130 eV and with an integration time of 11 min, normalized to the (00) spot (sample K2). The left image has a linear color scale capped at 0.1, highlighting the momentum resolution and the sharp diffraction spots. The right image illustrates the low noise floor after binning and the subtraction of a slowly varying background. Zoom-in displays the (00) spot with a linear color scale. (b) Region around (0.5 0.5), where a superstructure spot is expected. A linear intensity gradient was subtracted. (c) Histogram of the intensity within the red rectangle shown in the schematic diffraction pattern. The standard deviation σ_{noise} is 3.3×10^{-4}, and the detection threshold for a peak is defined by $3\sigma_{\text{noise}}$. (d) Experimental intensities of the main-lattice spots as well as expected strength of the CDW peaks, which is well above the detection threshold. The same analysis is done for a corresponding diffraction image at 80 eV and displayed in the lower half of the panel.

spots are above the detection threshold of $3\sigma_{\text{noise}}$, regardless of the two displayed electron energies. These spots should therefore be visible in both diffraction images. In particular, at an electron energy of 80 eV the expected peak strength of the (0.5 0.5) spots is roughly four times larger than our detection threshold, which suggests a reduced lattice distortion. Since the intensity of the superstructure peaks scales quadratically with the lattice distortion [see Fig. 2(b)], we estimate a PLD amplitude within the surface layer that is less than half its bulk value.

We discuss possible factors for a reduced strength of superstructure reflections in the context of the literature and our LEED experiments. First, due to the relaxation of surface bonds, the amplitude of lattice distortions can be reduced with respect to the bulk, and moderate deviations between bulk and surface CDW distortions have been previously observed in TaS_2 [44]. In comparison, the deduced reduction of the distortions by at least a factor of 2 in CsV_3Sb_5 appears to be more significant, which could point towards a different formation mechanism in these CDW materials. Second, the polarity of the cleaved surface must be considered, which changes depending on whether one is probing a predominantly Sb- or Cs-terminated surface, as the ionic bonds between antimony and alkali metal atoms are broken. Thus, the Sb-terminated surface is effectively hole doped. Recent termination-resolved ARPES studies consistently observed a CDW-induced splitting only on the alkali-terminated surfaces of all three AV_3Sb_5 compounds [45,46]. The findings are explained by the polar nature of the surface leading to energy shifts of key electronic bands. Moreover, this behavior is reminiscent of the asymmetry found between moderate hole or electron doping by Sn or Te substitution of antimony in bulk samples [47]: While in the latter case, the CDW state is largely preserved, hole doping rapidly suppresses the long-range charge order.

Our μm-beam LEED measurements imply a suppression of the CDW-coupled lattice distortion on Sb-terminated surfaces. Importantly, however, various STM studies were indeed able to observe a 2×2 motif on this termination, often superimposed with a uniaxial 1×4 modulation [20,32,34–36]. As we did not observe a unidirectional PLD either, the possible structural distortions of both surface modulations remain elusive. One might speculate whether the interplay of these two charge modulations may weaken their influence on atomic displacements. Our findings contribute to the ongoing debate, highlighting at least partially conflicting results that likely arise from the intricate band structure of CsV_3Sb_5. Taken together, these results emphasize the need for complementary experimental approaches, since electronic and structural manifestations of the CDW, as well as its bulk and surface properties, can differ significantly. Further LEED studies of CsV_3Sb_5 after cryogenic cleaving—which would also allow investigation of the cesium termination—or following the adsorption of cesium or different dopants could provide valuable insights to help resolve this puzzle. More generally, micron-scale surface-structural probing may help to elucidate origins of distinct charge density wave or pair density wave properties between the surface and the bulk of further correlated materials, such as UTe_2 [48–50] or hole-doped cuprates [51–55].

This work was funded by the European Research Council (ERC Advanced Grant "ULEEM," ID: 101055435) and the Deutsche Forschungsgemeinschaft (DFG, German Research Foundation) via resources from the Gottfried Wilhelm Leibniz Prize (RO 3936/4-1). F.K. gratefully acknowledges support from the Max Planck School of Photonics and I.V. acknowledges the HORIZON EUROPE MSCA Postdoctoral Fellowship (ID: 101065694). M.L.T. and A.A.H. acknowledge support by the DFG under CRC/TRR 288 (Project B03, Project No. 422213477). C.F. acknowledges support from the DFG under SFB 1143 (Project No. 247310070), the Würzburg-Dresden Cluster of Excellence on Complexity and Topology in Quantum Matter - ct.qmat (EXC 2147, Project No. 390858490), and FOR 5249 (QUAST, Project No. 449872909).

[1] B. R. Ortiz, L. C. Gomes, J. R. Morey, M. Winiarski, M. Bordelon, J. S. Mangum, I. W. H. Oswald, J. A. Rodriguez-Rivera, J. R. Neilson, S. D. Wilson, E. Ertekin, T. M. McQueen, and E. S. Toberer, New kagome prototype materials: Discovery of KV_3Sb_5, RbV_3Sb_5, and CsV_3Sb_5, Phys. Rev. Mater. **3**, 094407 (2019).

[2] S. D. Wilson and B. R. Ortiz, AV_3Sb_5 kagome superconductors, Nat. Rev. Mater. **9**, 420 (2024).

[3] Q. Yin, Z. Tu, C. Gong, Y. Fu, S. Yan, and H. Lei, Superconductivity and normal-state properties of kagome metal RbV_3Sb_5 single crystals, Chin. Phys. Lett. **38**, 037403 (2021).

[4] B. R. Ortiz, P. M. Sarte, E. M. Kenney, M. J. Graf, S. M. L. Teicher, R. Seshadri, and S. D. Wilson, Superconductivity in the $\mathbb{Z}_2$ kagome metal KV_3Sb_5, Phys. Rev. Mater. **5**, 034801 (2021).

[5] B. R. Ortiz, S. M. L. Teicher, Y. Hu, J. L. Zuo, P. M. Sarte, E. C. Schueller, A. M. M. Abeykoon, M. J. Krogstad, S. Rosenkranz, R. Osborn, R. Seshadri, L. Balents, J. He, and S. D. Wilson, CsV_3Sb_5: A $\mathbb{Z}_2$ topological kagome metal with a superconducting ground state, Phys. Rev. Lett. **125**, 247002 (2020).

[6] M. H. Christensen, T. Birol, B. M. Andersen, and R. M. Fernandes, Theory of the charge density wave in AV_3Sb_5 kagome metals, Phys. Rev. B **104**, 214513 (2021).

[7] H. Li, T. T. Zhang, T. Yilmaz, Y. Y. Pai, C. E. Marvinney, A. Said, Q. W. Yin, C. S. Gong, Z. J. Tu, E. Vescovo, C. S. Nelson, R. G. Moore, S. Murakami, H. C. Lei, H. N. Lee, B. J. Lawrie, and H. Miao, Observation of unconventional charge density wave without acoustic phonon anomaly in kagome superconductors AV_3Sb_5 ($A =$ Rb, Cs), Phys. Rev. X **11**, 031050 (2021).

[8] H. Li, G. Fabbris, A. H. Said, J. P. Sun, Y.-X. Jiang, J.-X. Yin, Y.-Y. Pai, S. Yoon, A. R. Lupini, C. S. Nelson, Q. W. Yin, C. S. Gong, Z. J. Tu, H. C. Lei, J.-G. Cheng, M. Z. Hasan, Z. Wang, B. Yan, R. Thomale, H. N. Lee *et al.*, Discovery of conjoined charge density waves in the kagome superconductor CsV_3Sb_5, Nat. Commun. **13**, 6348 (2022).

[9] F. Kaboudvand, S. M. L. Teicher, S. D. Wilson, R. Seshadri, and M. D. Johannes, Fermi surface nesting and the Lindhard response function in the kagome superconductor CsV_3Sb_5, Appl. Phys. Lett. **120**, 111901 (2022).

[10] B. R. Ortiz, S. M. L. Teicher, L. Kautzsch, P. M. Sarte, N. Ratcliff, J. Harter, J. P. C. Ruff, R. Seshadri, and S. D. Wilson, Fermi surface mapping and the nature of charge-density-wave order in the kagome superconductor CsV_3Sb_5, Phys. Rev. X **11**, 041030 (2021).

[11] Q. Stahl, D. Chen, T. Ritschel, C. Shekhar, E. Sadrollahi, M. C. Rahn, O. Ivashko, M. v. Zimmermann, C. Felser, and J. Geck, Temperature-driven reorganization of electronic order in CsV_3Sb_5, Phys. Rev. B **105**, 195136 (2022).

[12] L. Kautzsch, B. R. Ortiz, K. Mallayya, J. Plumb, G. Pokharel, J. P. C. Ruff, Z. Islam, E.-A. Kim, R. Seshadri, and S. D. Wilson, Structural evolution of the kagome superconductors AV_3Sb_5

(A = K, Rb, and Cs) through charge density wave order, Phys. Rev. Mater. **7**, 024806 (2023).

[13] J. Frassineti, P. Bonfà, G. Allodi, E. Garcia, R. Cong, B. R. Ortiz, S. D. Wilson, R. De Renzi, V. F. Mitrović, and S. Sanna, Microscopic nature of the charge-density wave in the kagome superconductor RbV_3Sb_5, Phys. Rev. Res. **5**, L012017 (2023).

[14] Y. Wang, T. Wu, Z. Li, K. Jiang, and J. Hu, Structure of the kagome superconductor CsV_3Sb_5 in the charge density wave state, Phys. Rev. B **107**, 184106 (2023).

[15] Q. Xiao, Y. Lin, Q. Li, X. Zheng, S. Francoual, C. Plueckthun, W. Xia, Q. Qiu, S. Zhang, Y. Guo, J. Feng, and Y. Peng, Coexistence of multiple stacking charge density waves in kagome superconductor CsV_3Sb_5, Phys. Rev. Res. **5**, L012032 (2023).

[16] J. Plumb, A. C. Salinas, K. Mallayya, E. Kisiel, F. B. Carneiro, R. Gomez, G. Pokharel, E.-A. Kim, S. Sarker, Z. Islam, S. Daly, and S. D. Wilson, Phase-separated charge order and twinning across length scales in CsV_3Sb_5, Phys. Rev. Mater. **8**, 093601 (2024).

[17] C. Mielke, D. Das, J.-X. Yin, H. Liu, R. Gupta, Y.-X. Jiang, M. Medarde, X. Wu, H. C. Lei, J. Chang, P. Dai, Q. Si, H. Miao, R. Thomale, T. Neupert, Y. Shi, R. Khasanov, M. Z. Hasan, H. Luetkens, and Z. Guguchia, Time-reversal symmetry-breaking charge order in a kagome superconductor, Nature (London) **602**, 245 (2022).

[18] M. H. Christensen, T. Birol, B. M. Andersen, and R. M. Fernandes, Loop currents in AV_3Sb_5 kagome metals: Multipolar and toroidal magnetic orders, Phys. Rev. B **106**, 144504 (2022).

[19] Y.-X. Jiang, J.-X. Yin, M. M. Denner, N. Shumiya, B. R. Ortiz, G. Xu, Z. Guguchia, J. He, M. S. Hossain, X. Liu, J. Ruff, L. Kautzsch, S. S. Zhang, G. Chang, I. Belopolski, Q. Zhang, T. A. Cochran, D. Multer, M. Litskevich, Z.-J. Cheng *et al.*, Unconventional chiral charge order in kagome superconductor KV_3Sb_5, Nat. Mater. **20**, 1353 (2021).

[20] N. Shumiya, M. S. Hossain, J.-X. Yin, Y.-X. Jiang, B. R. Ortiz, H. Liu, Y. Shi, Q. Yin, H. Lei, S. S. Zhang, G. Chang, Q. Zhang, T. A. Cochran, D. Multer, M. Litskevich, Z.-J. Cheng, X. P. Yang, Z. Guguchia, S. D. Wilson, and M. Z. Hasan, Intrinsic nature of chiral charge order in the kagome superconductor RbV_3Sb_5, Phys. Rev. B **104**, 035131 (2021).

[21] Y. Xiang, Q. Li, Y. Li, W. Xie, H. Yang, Z. Wang, Y. Yao, and H.-H. Wen, Twofold symmetry of c-axis resistivity in topological kagome superconductor CsV_3Sb_5 with in-plane rotating magnetic field, Nat. Commun. **12**, 6727 (2021).

[22] M. L. Kiesel, C. Platt, and R. Thomale, Unconventional Fermi surface instabilities in the kagome Hubbard model, Phys. Rev. Lett. **110**, 126405 (2013).

[23] D. R. Saykin, C. Farhang, E. D. Kountz, D. Chen, B. R. Ortiz, C. Shekhar, C. Felser, S. D. Wilson, R. Thomale, J. Xia, and A. Kapitulnik, High resolution polar Kerr effect studies of CsV_3Sb_5: Tests for time-reversal symmetry breaking below the charge-order transition, Phys. Rev. Lett. **131**, 016901 (2023).

[24] W. Liège, Y. Xie, D. Bounoua, Y. Sidis, F. Bourdarot, Y. Li, Z. Wang, J.-X. Yin, P. Dai, and P. Bourges, Search for orbital magnetism in the kagome superconductor CsV_3Sb_5 using neutron diffraction, Phys. Rev. B **110**, 195109 (2024).

[25] H. Li, S. Wan, H. Li, Q. Li, Q. Gu, H. Yang, Y. Li, Z. Wang, Y. Yao, and H.-H. Wen, No observation of chiral flux current in the topological kagome metal CsV_3Sb_5, Phys. Rev. B **105**, 045102 (2022).

[26] H. J. Elmers, O. Tkach, Y. Lytvynenko, P. Yogi, M. Schmitt, D. Biswas, J. Liu, S. V. Chernov, Q. Nguyen, M. Hoesch, D. Kutnyakhov, N. Wind, L. Wenthaus, M. Scholz, K. Rossnagel, A. Gloskovskii, C. Schlueter, A. Winkelmann, A.-A. Haghighirad, T.-L. Lee *et al.*, Chirality in the kagome metal CsV_3Sb_5, Phys. Rev. Lett. **134**, 096401 (2025).

[27] M. Frachet, L. Wang, W. Xia, Y. Guo, M. He, N. Maraytta, R. Heid, A.-A. Haghighirad, M. Merz, C. Meingast, and F. Hardy, Colossal c-axis response and lack of rotational symmetry breaking within the kagome planes of the CsV_3Sb_5 superconductor, Phys. Rev. Lett. **132**, 186001 (2024).

[28] E. Uykur, B. R. Ortiz, O. Iakutkina, M. Wenzel, S. D. Wilson, M. Dressel, and A. A. Tsirlin, Low-energy optical properties of the nonmagnetic kagome metal CsV_3Sb_5, Phys. Rev. B **104**, 045130 (2021).

[29] X. Zhou, Y. Li, X. Fan, J. Hao, Y. Dai, Z. Wang, Y. Yao, and H.-H. Wen, Origin of charge density wave in the kagome metal CsV_3Sb_5 as revealed by optical spectroscopy, Phys. Rev. B **104**, L041101 (2021).

[30] G. He, L. Peis, E. F. Cuddy, Z. Zhao, D. Li, Y. Zhang, R. Stumberger, B. Moritz, H. Yang, H. Gao, T. P. Devereaux, and R. Hackl, Anharmonic strong-coupling effects at the origin of the charge density wave in CsV_3Sb_5, Nat. Commun. **15**, 1895 (2024).

[31] M. Kang, S. Fang, J.-K. Kim, B. R. Ortiz, S. H. Ryu, J. Kim, J. Yoo, G. Sangiovanni, D. D. Sante, B.-G. Park, C. Jozwiak, A. Bostwick, E. Rotenberg, E. Kaxiras, S. D. Wilson, J.-H. Park, and R. Comin, Twofold van Hove singularity and origin of charge order in topological kagome superconductor CsV_3Sb_5, Nat. Phys. **18**, 301 (2022).

[32] Z. Liang, X. Hou, F. Zhang, W. Ma, P. Wu, Z. Zhang, F. Yu, J.-J. Ying, K. Jiang, L. Shan, Z. Wang, and X.-H. Chen, Three-dimensional charge density wave and surface-dependent vortex-core states in a kagome superconductor CsV_3Sb_5, Phys. Rev. X **11**, 031026 (2021).

[33] K. Nakayama, Y. Li, T. Kato, M. Liu, Z. Wang, T. Takahashi, Y. Yao, and T. Sato, Multiple energy scales and anisotropic energy gap in the charge-density-wave phase of the kagome superconductor CsV_3Sb_5, Phys. Rev. B **104**, L161112 (2021).

[34] H. Chen, H. Yang, B. Hu, Z. Zhao, J. Yuan, Y. Xing, G. Qian, Z. Huang, G. Li, Y. Ye, S. Ma, S. Ni, H. Zhang, Q. Yin, C. Gong, Z. Tu, H. Lei, H. Tan, S. Zhou, C. Shen *et al.*, Roton pair density wave in a strong-coupling kagome superconductor, Nature (London) **599**, 222 (2021).

[35] H. Zhao, H. Li, B. R. Ortiz, S. M. L. Teicher, T. Park, M. Ye, Z. Wang, L. Balents, S. D. Wilson, and I. Zeljkovic, Cascade of correlated electron states in the kagome superconductor CsV_3Sb_5, Nature (London) **599**, 216 (2021).

[36] Z. Wang, Y.-X. Jiang, J.-X. Yin, Y. Li, G.-Y. Wang, H.-L. Huang, S. Shao, J. Liu, P. Zhu, N. Shumiya, M. S. Hossain, H. Liu, Y. Shi, J. Duan, X. Li, G. Chang, P. Dai, Z. Ye, G. Xu, Y. Wang *et al.*, Electronic nature of chiral charge order in the kagome superconductor CsV_3Sb_5, Phys. Rev. B **104**, 075148 (2021).

[37] S. Vogelgesang, G. Storeck, J. G. Horstmann, T. Diekmann, M. Sivis, S. Schramm, K. Rossnagel, S. Schäfer, and C. Ropers, Phase ordering of charge density waves traced by ultrafast low-energy electron diffraction, Nat. Phys. **14**, 184 (2018).

[38] See Supplemental Material at http://link.aps.org/supplemental/10.1103/PhysRevB.111.L140101 for further information on crystal growth, the LEED setup and image analysis used, and additional experimental measurements and dynamical LEED calculations.

[39] J. Yu, Z. Xu, K. Xiao, Y. Yuan, Q. Yin, Z. Hu, C. Gong, Y. Guo, Z. Tu, P. Tang, H. Lei, Q.-K. Xue, and W. Li, Evolution of electronic structure in pristine and Rb-reconstructed surfaces of kagome metal RbV_3Sb_5, Nano Lett. **22**, 918 (2022).

[40] V. Blum and K. Heinz, Fast LEED intensity calculations for surface crystallography using Tensor LEED, Comput. Phys. Commun. **134**, 392 (2001).

[41] H. Miao, H. X. Li, W. R. Meier, A. Huon, H. N. Lee, A. Said, H. C. Lei, B. R. Ortiz, S. D. Wilson, J. X. Yin, M. Z. Hasan, Z. Wang, H. Tan, and B. Yan, Geometry of the charge density wave in the kagome metal AV_3Sb_5, Phys. Rev. B **104**, 195132 (2021).

[42] H. Tan, Y. Liu, Z. Wang, and B. Yan, Charge density waves and electronic properties of superconducting kagome metals, Phys. Rev. Lett. **127**, 046401 (2021).

[43] In principle, the detector area, where the background is evaluated, includes the region of possible superstructure peaks. However, due to the small number of pixels they would cover (less than 1% of the selected area), this does not affect the standard deviation.

[44] G. von Witte, T. Kißlinger, J. G. Horstmann, K. Rossnagel, M. A. Schneider, C. Ropers, and L. Hammer, Surface structure and stacking of the commensurate $(\sqrt{13}\times\sqrt{13})R13.9^\circ$ charge density wave phase of $1T-TaS_2(0001)$, Phys. Rev. B **100**, 155407 (2019).

[45] T. Kato, Y. Li, K. Nakayama, Z. Wang, S. Souma, M. Kitamura, K. Horiba, H. Kumigashira, T. Takahashi, and T. Sato, Polarity-dependent charge density wave in the kagome superconductor CsV_3Sb_5, Phys. Rev. B **106**, L121112 (2022).

[46] T. Kato, Y. Li, M. Liu, K. Nakayama, Z. Wang, S. Souma, M. Kitamura, K. Horiba, H. Kumigashira, T. Takahashi, Y. Yao, and T. Sato, Surface-termination-dependent electronic states in kagome superconductors AV_3Sb_5 (A = K, Rb, Cs) studied by micro-ARPES, Phys. Rev. B **107**, 245143 (2023).

[47] A. N. C. Salinas, B. R. Ortiz, C. Bales, J. Frassineti, V. F. Mitrović, and S. D. Wilson, Electron-hole asymmetry in the phase diagram of carrier-tuned CsV_3Sb_5, Front. Electron. Mater. **3**, 1257490 (2023).

[48] A. Aishwarya, J. May-Mann, A. Raghavan, L. Nie, M. Romanelli, S. Ran, S. R. Saha, J. Paglione, N. P. Butch, E. Fradkin, and V. Madhavan, Magnetic-field-sensitive charge density waves in the superconductor UTe_2, Nature (London) **618**, 928 (2023).

[49] F. Theuss, A. Shragai, G. Grissonnanche, L. Peralta, G. de la Fuente Simarro, I. M. Hayes, S. R. Saha, Y. S. Eo, A. Suarez, A. C. Salinas, G. Pokharel, S. D. Wilson, N. P. Butch, J. Paglione, and B. J. Ramshaw, Absence of a bulk thermodynamic phase transition to a density wave phase in UTe_2, Phys. Rev. B **110**, 144507 (2024).

[50] C. S. Kengle, D. Chaudhuri, X. Guo, T. A. Johnson, S. Bettler, W. Simeth, M. J. Krogstad, Z. Islam, S. Ran, S. R. Saha, J. Paglione, N. P. Butch, E. Fradkin, V. Madhavan, and P. Abbamonte, Absence of a bulk signature of a charge density wave in hard x-ray measurements of UTe_2, Phys. Rev. B **110**, 145101 (2024).

[51] S. D. Edkins, A. Kostin, K. Fujita, A. P. Mackenzie, H. Eisaki, S. Uchida, S. Sachdev, M. J. Lawler, E.-A. Kim, J. C. S. Davis, and M. H. Hamidian, Magnetic field–induced pair density wave state in the cuprate vortex halo, Science **364**, 976 (2019).

[52] I. Maggio-Aprile, T. P. Singar, C. Berthod, T. Gazdić, J. Bruér, and C. Renner, Vortex-core spectroscopy of d-wave cuprate high-temperature superconductors, Physica C: Supercond. Appl. **615**, 1354386 (2023).

[53] E. H. Da Silva Neto, P. Aynajian, A. Frano, R. Comin, E. Schierle, E. Weschke, A. Gyenis, J. Wen, J. Schneeloch, Z. Xu, S. Ono, G. Gu, M. Le Tacon, and A. Yazdani, Ubiquitous interplay between charge ordering and high-temperature superconductivity in cuprates, Science **343**, 393 (2014).

[54] I. Vinograd, R. Zhou, M. Hirata, T. Wu, H. Mayaffre, S. Krämer, R. Liang, W. N. Hardy, D. A. Bonn, and M.-H. Julien, Locally commensurate charge-density wave with three-unit-cell periodicity in $YBa_2Cu_3O_y$, Nat. Commun. **12**, 3274 (2021).

[55] E. Blackburn, O. Ivashko, E. Campillo, M. von Zimmermann, R. Liang, D. A. Bonn, W. N. Hardy, J. Chang, E. M. Forgan, and S. M. Hayden, Searching for the signature of a pair density wave in $YBa_2Cu_3O_{6.67}$ using high energy x-ray diffraction, arXiv:2310.18302.